Control of Unsteady Solidification via Optimized Magnetic Fields

Marcelo J. Colaço, George S. Dulikravich and Thomas J. Martin

Author Queries

AQ1 Au: Please provide better quality artworks.
AQ2 Au: Please supply location.
AQ3 Au: Location OK as added.

Materials and Manufacturing Processes, 20: 1–25, 2005

ISSN: 1042-6914 print/1532-2475 online
DOI: 10.1081/AMP-200053456

Taylor & Francis
Taylor & Francis Group

CONTROL OF UNSTEADY SOLIDIFICATION VIA OPTIMIZED MAGNETIC FIELDS

Marcelo J. Colaço
Military Institute of Engineering (IME), Mechanical and Materials Engineering Department (DE/4), Praca General Tiburcio, Rio de Janeiro, Brazil

George S. Dulikravich
Department of Mechanical and Materials Engineering, Florida International University, Miami, Florida, USA

Thomas J. Martin
Pratt & Whitney Engine Company, Turbine Discipline Engineering and Optimization Group, East Hartford, CT, USA

This article presents a numerical procedure for automatically controlling desired features of a melt undergoing solidification by applying an external magnetic field whose time-varying intensity and spatial distribution are obtained by the use of a hybrid optimization algorithm. The intensities of the magnets along the boundaries of the container were discretized by using B-splines. The inverse problem is then formulated to find the magnetic boundary conditions (the coefficients of the B-splines) in such a way that the gradients of temperature along the gravity direction are minimized at each instant as the solidification front advances through a moving melt. For this task, a hybrid optimization code was used that automatically switches among the following six optimization modules; the Davidon-Fletcher-Powell (DFP) gradient method, a genetic algorithm (GA), the Nelder-Mead (NM) simplex method, quasi-Newton algorithm of Pshenichny-Danilin (LM), differential evolution (DE), and sequential quadratic programming (SQP). Transient Navier-Stokes and Maxwell's equations were discretized by using a finite volume method in a generalized curvilinear nonorthogonal coordinate system. For the phase change problems, an enthalpy formulation was used. The computer code was validated against analytical and numerical benchmark results with very good agreements in both cases.

Key Words: Flow control; Genetic algorithm; Hybrid optimization; Magnetohydrodynamics; Smart manufacturing; Solidification.

Received April 6, 2004; Accepted November 8, 2004
Address correspondence to George S. Dulikravich, Department of Mechanical and Materials Engineering, MAIDROC Laboratory, EC 3474, Florida International University, Miami, FL 33027, USA; Fax: +1 305-348-6007; E-mail: dulikrav@fiu.edu

NOMENCLATURE

C_P	specific heat at constant pressure
B_x	magnetic flux component in x-direction
B_y	magnetic flux component in y-direction
g	acceleration of the gravity
Gr	Grashoff number
f	solid fraction
k	thermal conductivity
L	latent heat of solidification/melting
h	enthalpy
Ht	Hartmann number
n	partition coefficient in Scheil's Eq. (5)
p	pressure
Pr	Prandtl number
Ra	Rayleigh number
t	time
T	temperature
u	velocity component in x-direction
v	velocity component in y-direction
x, y	Cartesian coordinates

Greek letters

α	thermal diffusivity
β	thermal expansion coefficient
μ	fluid viscosity
μ_m	magnetic permeability
σ	electric conductivity
ν	kinematic viscosity

Subscripts

l	liquid value
m	melting value
s	solid value
0	reference value

1. INTRODUCTION

In some metallurgical system, external stirring is applied to have preferred morphology and reduced solute microsegregation. During a controlled solidification process from a melt, it is important to understand the process of solid phase formation. This process cannot be effectively controlled in strong heat transfer, except if influenced by a global body force. For example, if an external magnetic field is applied, the melt flow field will respond and the solid/liquid front shape and its speed could be manipulated nonintrusively [1–6]. To minimize residual thermal stresses in the solid accrued during solidification, it is desirable to make

the melt/solid interface as flat as possible. In addition, it is often desirable to minimize the transport of impurities from walls of the solidification container to the mushy region and eventually into the accruing solid phase. If the intensity of thermal convection is minimized in appropriate parts of the melt flow field, then solidification will become an almost convection-free process.

The first objective of this work is to present some results obtained with a time-accurate code capable of simulating magnetohydrodynamic (MHD) flows with phase change. The second objective is to combine this analysis code and an optimization code to demonstrate unsteady control of the natural convection effects in a cavity filled with a solidifying melt. By actively controlling the natural convection effects, it should be possible to produce solids with desired shapes having lower thermal stresses than those obtained in a presence of very strong thermal buoyancy forces.

Two test cases are presented. The first involves only natural convection with a Rayleigh number equal to 10^5, whereas the second involves phase change in the presence of a natural convection with a Rayleigh number equal to 10^5. Applying an optimized magnetic field obtained by the use of a hybrid optimizer reduced the natural convection effects. The difference between this and our previous work [7] is in the numerical method for dealing with the nonlinear MHD model. The current method is able to use realistic values of physical properties, especially for the magnetic Prandtl number and is also time-accurate. The method was validated against transient and steady-state analytic solutions and then used in an unsteady magnetic field optimization study.

2. MAGNETOHYDRODYNAMIC (MHD) MODEL

The physical problem considered here involves the laminar magneto-hydrodynamic natural convection of an incompressible Newtonian fluid. The fluid physical properties are assumed constant within each phase (solid or liquid) and linearly varying in the mushy region between the two phases. The energy source term resulting from viscous dissipation is neglected, and buoyancy effects are approximated by the Boussinesq hypothesis. The modifications to the Navier-Stokes equations for the MHD fluid flow with heat transfer come from the electromagnetic force in the fluid where all induced electric field terms have been neglected [3]. Then, the Navier-Stokes and the Maxwell equations can be written for the Cartesian coordinate system in two dimensions as

$$\frac{\partial Q}{\partial t} + \frac{\partial E}{\partial x} + \frac{\partial F}{\partial y} = S \tag{1}$$

where

$$Q = \lambda\phi \tag{2a}$$

$$E = \lambda u\phi^* - \Gamma\frac{\partial \phi^{***}}{\partial x} \tag{2b}$$

$$F = \lambda v\phi^{**} - \Gamma\frac{\partial \phi^{***}}{\partial y} \tag{2c}$$

Table 1 Parameters for the Navier-Stokes and Maxwell equations

Conservation of	λ	ϕ	ϕ^*	ϕ^{**}	ϕ^{***}	Γ	S
Mass	ρ	1	1	1	1	0	0
x-momentum	ρ	u	u	u	u	μ	$-\frac{\partial P}{\partial x} - \frac{B_y}{\mu_m}\left[\frac{\partial B_y}{\partial x} - \frac{\partial B_x}{\partial y}\right]$
y-momentum	ρ	v	v	v	v	μ	$-\frac{\partial P}{\partial y} - \rho g[1-\beta(T-T_0)] + \frac{B_y}{\mu_m}\left[\frac{\partial B_y}{\partial x} - \frac{\partial B_x}{\partial y}\right]$
Energy	ρ	h	h	h	T	k	$\frac{C_P}{\sigma\mu_m^2}\left[\frac{\partial B_y}{\partial x} - \frac{\partial B_x}{\partial y}\right]^2$
Magnetic flux in x-direction	1	B_x	0	B_x	B_x	$\frac{1}{\mu_m\sigma}$	$\frac{\partial(uB_y)}{\partial y}$
Magnetic flux in y-direction	1	B_y	B_y	0	B_y	$\frac{1}{\mu_m\sigma}$	$\frac{\partial(vB_x)}{\partial x}$

The values of S, λ, ϕ, ϕ^*, ϕ^{**}, ϕ^{***} and Γ are given in Table 1 for the equations T1
of conservation of mass, x-momentum, y-momentum, energy, magnetic flux in the x-direction, and magnetic flux in the y-direction.

Note that we used the Boussinesq approximation for the variation of the density with temperature in the y-momentum conservation equation. Also note that in the energy conservation equation, the term C_PT was replaced by the enthalpy, h, per unit mass. This is useful for problems dealing with phase change where we used the enthalpy method [8]. The above equations were transformed from the physical Cartesian (x, y) coordinates to the curvilinear boundary-conforming computational coordinate system (ξ, η) and solved by the finite volume method. The SIMPLEC method [9] was used to solve velocity-pressure coupling problem. The WUDS interpolation scheme [10] was used to obtain the values of u, v, h, B_x and B_y as well as their derivatives at the interfaces of each control volume. The resulting linear system was solved by the GMRES method.

3. PHASE CHANGE MODEL

In this article, we used the enthalpy method [8] to deal with the phase change problem. In this method, the energy equation appears as a mixed enthalpy-temperature equation. Thus, we must obtain some relationship between the temperature and the enthalpy to be used in the energy equation. For a binary alloy, if $h < h_{\text{solid}}$, we have

$$T = \frac{h}{C_{Ps}} \tag{3a}$$

or, if $h > h_{\text{liquid}}$

$$T = \frac{h + T_s(C_{Pl} - C_{Ps}) - L}{C_{Pl}} \tag{3b}$$

or yet, if $h_{\text{solid}} < h < h_{\text{liquid}}$

$$T = T_s = T_l = T_{melt} \tag{3c}$$

For a mixture, we have a range of temperatures where the solidification might occur. Then, if $h_{\text{solid}} < h < h_{\text{liquid}}$,

$$T = \frac{h + [T_s(C_{Pl} - C_{Ps}) - L](1 - f)}{C_{Pl} + f(C_{Ps} - C_{Pl})} \tag{4}$$

where the solid fraction f is given by the Scheil's model [11]

$$f = 1 - \left(\frac{T_s - T}{T_s - T_l}\right)^{1/(n-1)} \tag{5}$$

In the above equation, we set the partition coefficient $n = 2$, which reduces the Scheil's model to the linear interpolation function. Note that if $T < T_{\text{solid}}$, f must be set to unity and, if $T > T_{\text{liquid}}$, f must be set to zero. The magnetic and thermal properties were approximated as linear functions within the mushy region ($T_{\text{solid}} < T < T_{\text{liquid}}$) and kept constant within each phase. Thus, in the mushy region

$$\psi = f\psi_s + (1 - f)\psi_l \tag{6}$$

where ψ represents the density, thermal conductivity, viscosity, magnetic permeability and electric conductivity. For the viscosity of the solid phase we used

$$\frac{\mu_s}{\mu_l} \geq 10^6 \tag{7}$$

and for the specific heat at constant pressure within the mushy region, we used the thermodynamic property

$$C_P = \frac{\partial h}{\partial T} \approx \frac{\sqrt{\left(\frac{\partial h}{\partial x}\right)^2 + \left(\frac{\partial h}{\partial y}\right)^2}}{\sqrt{\left(\frac{\partial T}{\partial x}\right)^2 + \left(\frac{\partial T}{\partial y}\right)^2}} \tag{8}$$

Note that if we are dealing with a mixture, the enthalpy is a function of the temperature, which is a function of the solid fraction that is itself a function of the temperature. Thus, if $h_{\text{solid}} < h < h_{\text{liquid}}$, we must solve a nonlinear system for T. From Eqs. (4) and (5) it follows that

$$T - \frac{h + [T_s(C_{Pl} - C_{Ps}) - L]\left[\left(\frac{T_s - T}{T_s - T_l}\right)^{1/(n-1)}\right]}{C_{Pl} + \left[1 - \left(\frac{T_s - T}{T_s - T_l}\right)^{1/(n-1)}\right](C_{Ps} - C_{Pl})} = 0 \tag{9}$$

which can be solved for T by the secant method. It should be pointed out that in this article we have not considered any sink for the momentum due to viscous dissipation in the mushy region. We have also not considered dynamic grid

clustering with respect to the solid/melt interface to resolve the details of the mushy region.

4. VALIDATION OF THE MHD SOLIDIFICATION ANALYSIS CODE

The analysis code was validated against available analytical and experimental benchmark results. For problems without phase change and without magnetic fields, other validations can be found [12, 13]. Given below are presentations of the validations for phase change problems and for problems with magnetic fields.

4.1. Pouiseuille-Hartmann Flow

The Pouiseuille-Hartmann flow is a one-dimensional flow of an electrically conducting, incompressible, viscous fluid between two stationary infinite parallel plates with a uniform external magnetic field applied orthogonal to the plates. See the geometry in Fig. 1, where the fluid enters the domain at $x = 0$ and the uniform magnetic field is applied orthogonal to the walls located at $y = 0$ and $y = 2\mathrm{H}$. F1

The analytical solution for the velocity field is given as [14]

$$u(y) = \frac{dP}{dx}\frac{H^2}{\mu}\left[\frac{\cosh(Ht) - \cosh\left(Ht\frac{y}{H}\right)}{Ht\sinh(Ht)}\right] \tag{10}$$

where the Hartmann number is defined as:

$$Ht = B_0 H_0\sqrt{\frac{\sigma}{\mu}} \tag{11}$$

Let us consider the following properties for silicon.

$\rho = 2550\,\mathrm{kg\,m^{-2}}$
$C_P = 1059\,\mathrm{J\,kg^{-1}\,K^{-1}}$
$k = 64\,\mathrm{W\,m^{-1}\,K^{-1}}$
$\mu = 7.018 \times 10^{-4}\,\mathrm{kg\,m^{-1}\,s^{-1}}$
$\sigma = 12.3 \times 10^{5}\,\Omega^{-1}\,\mathrm{m^{-1}}$
$\beta = 1.4 \times 10^{-4}\,\mathrm{K^{-1}}$
$\mu_m = 1.2566 \times 10^{-5}\,\mathrm{T\,m\,A^{-1}}$

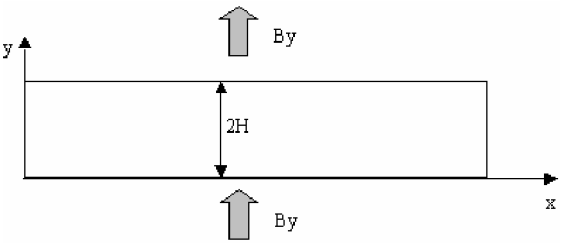

Figure 1 Geometry for the Poiseuille-Hartmann flow.

Table 2 Hartmann numbers and magnetic fields for the three Pouiseuille-Hartmann flow test cases

Test case no.	Ht	$B_0(T)$
1	1.0	2.3887×10^{-4}
2	5.0	1.1943×10^{-3}
3	10.0	2.3887×10^{-3}

By choosing the channel half-width as $H_0 = 0.1\,\text{m}$, we have evaluated the accuracy of the MHD code against the following three Pouiseuille-Hartmann flow test cases (Table 2). T2

Figures 2, 3, and 4 show the comparison between the numerically obtained and the analytical results for a non-uniform grid with 80×80 quadrilateral cells clustered symmetrically towards the walls. One can note that the analytical and numerical results have excellent agreement, with an error less than one percent close to the walls and less than 0.05 percent at the center of the channel. F2–F4

4.2. Unsteady Solidification/Melting in a Heat Conduction Problem

Let us consider the following one-dimensional unsteady heat conduction problem with phase change in a semi-infinite medium (Fig. 5), where the coordinate $x = 0$ is kept at a temperature $T_0 < T_m$ and the infinity $x \to \infty$ is kept at $T_i > T_m$. The temperatures within each phase T_s and T_l vary with position x and with time t. The interface between the two phases vary its position with time as a function $s(t)$. F5

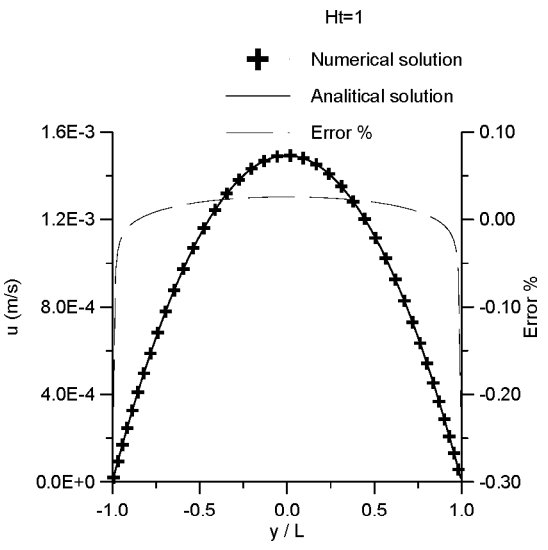

Figure 2 Test case no. 1 for the Poiseuille-Hartmann flow.

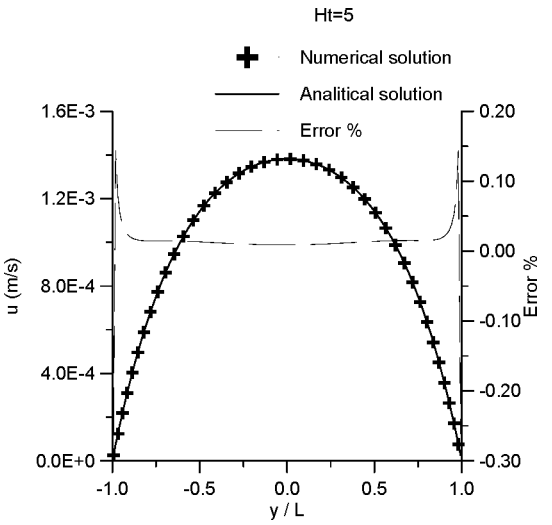

Figure 3 Test case no. 2 for the Poiseuille-Hartmann flow.

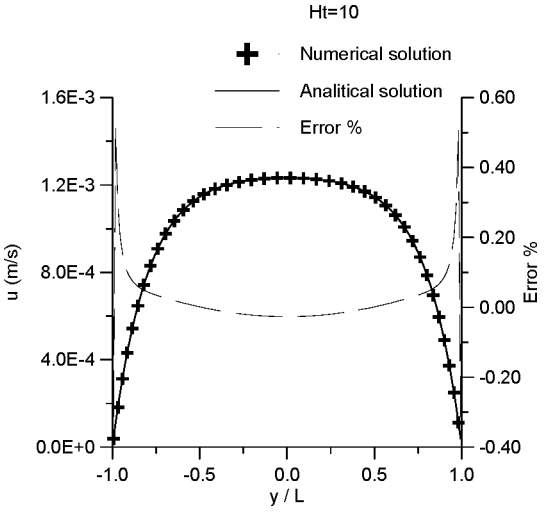

Figure 4 Test case no. 3 for the Poiseuille-Hartmann flow.

The mathematical formulation of this problem for the solid phase is given as

$$\frac{\partial^2 T_s}{\partial x^2} = \frac{1}{\alpha_s}\frac{\partial T_s(x,t)}{\partial t} \quad \text{in } 0 < x < s(t),\ t > 0 \tag{12a}$$

$$T_s(x,t) = T_0 \quad \text{at } x = 0,\ t > 0 \tag{12b}$$

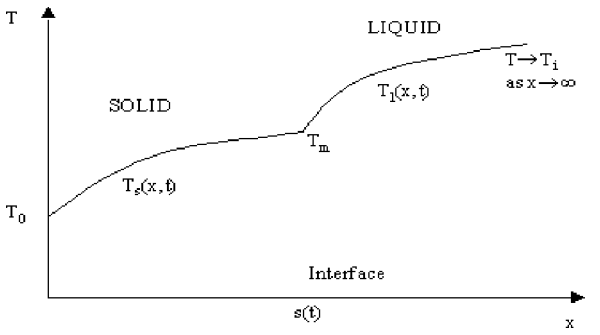

Figure 5 Phase change in a semi-infinite medium.

and for the liquid phase as

$$\frac{\partial^2 T_l}{\partial x^2} = \frac{1}{\alpha_l}\frac{\partial T_l(x,t)}{\partial t} \quad \text{in } s(t) < x < \infty, \ \ t > 0 \tag{13a}$$

$$T_l(x,t) = T_i \quad \text{as } x \to \infty, \ \ t > 0 \tag{13b}$$

$$T_l(x,t) = T_0 \quad \text{for } t = 0, \ \ x > 0 \tag{13c}$$

The coupling conditions at the interface $x = s(t)$ are

$$T_s(x,t) = T_l(x,t) = T_m \qquad \text{at } x = s(t), \ \ t > 0 \tag{14a}$$

$$k_s\frac{\partial T_s}{\partial x} - k_l\frac{\partial T_l}{\partial x} = \rho L\frac{ds(t)}{dt} \qquad \text{at } x = s(t), \ \ t > 0 \tag{14b}$$

The analytical solution is given as [15]

$$T_s(x,t) = (T_m - T_0)\frac{erf\,[x/(2\alpha_s t)^{1/2}]}{erf(\lambda)} + T_0 \tag{15a}$$

$$T_l(x,t) = (T_m - T_i)\frac{erfc[x/(2\alpha_l t)^{1/2}]}{erf\,[\lambda(\alpha_s/\alpha_l)^{1/2}]} + T_i \tag{15b}$$

where λ is given as a transcendental expression by

$$\frac{e^{-\lambda^2}}{erf(\lambda)} + \frac{k_l}{k_s}\left(\frac{\alpha_l}{\alpha_s}\right)^{1/2}\frac{T_m - T_i}{T_m - T_0}\frac{e^{-\lambda^2(\alpha_s/\alpha_l)}}{erfc[\lambda(\alpha_s/\alpha_l)^{1/2}]} = \frac{\lambda L\sqrt{\pi}}{C_{Ps}(T_m - T_0)} \tag{16}$$

The instantaneous solid-liquid interface location $s(t)$ is given by

$$s(t) = 2\lambda(\alpha, t)^{1/2} \tag{17}$$

where α is the thermal diffusivity defined as

$$\alpha = \frac{k}{\rho C_P} \tag{18}$$

Table 3 Physical properties of liquid and solid silicon

$\rho = \text{constant} = 2550\,\text{kg m}^{-3}$	$L = 1.803 \times 10^6\,\text{J kg}^{-1}$
$k_l = 64\,\text{W m}^{-1}\,\text{K}^{-1}$	$C_{Pl} = 1059\,\text{J kg}^{-1}\,\text{K}^{-1}$
$k_s = 22\,\text{W m}^{-1}\,\text{K}^{-1}$	$C_{Ps} = 1038\,\text{J kg}^{-1}\,\text{K}^{-1}$

The one-dimensional unsteady heat conduction problem with phase change was approximated as a two-dimensional plate where the top and bottom surfaces were kept insulated to reduce the problem from the two-dimensional to the one-dimensional case. The right wall boundary condition, located at $x = 3.0\,\text{m}$, was considered to be at the "infinity" and kept at $T_i = 1688.0\,\text{K}$. The left wall boundary condition was equal to the initial boundary condition $T_0 = 1676.0\,\text{K}$. The melting temperature was $T_m = 1683.0\,\text{K}$. For this problem, we used silicon with the following properties (Table 3). T3

Figures 6 and 7 show the comparisons between the numerically obtained and the analytical results at two different times, where the temperature is plotted as a function of the distance x. The point where the curve changes its slope represents the place where the solid-liquid interface is located. One can see the excellent agreement between the numerical and the analytic solutions, showing the good accuracy of the method for transient heat conduction problems with phase change. It is interesting to note that, as the interface moves toward the right boundary, the current numerical results start to slightly deviate from the analytical results in the region close to the right boundary (Fig. 7). This is due to the fact that we have approximated the infinity with a finite value of x at the right end of the plate. F6–F7

4.3. Unsteady Solidification/Melting in a Heat Convection Problem

To validate the transient solidification simulation code in a problem involving natural convection without a magnetic field, we compared the present code with the

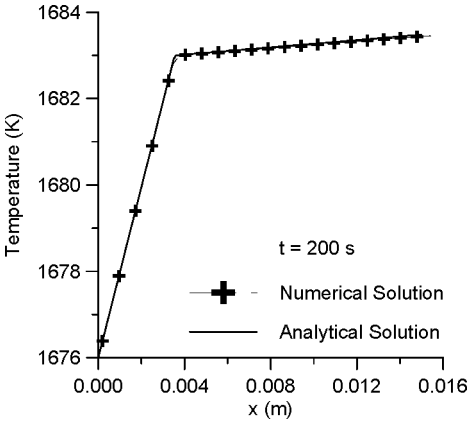

Figure 6 Unsteady heat conduction phase change problem ($t = 200\,\text{s}$).

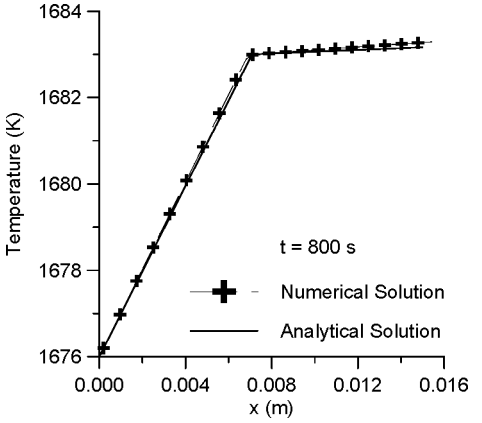

Figure 7 Unsteady heat conduction phase change problem ($t = 800$ s).

results published by Bertrand et al. [16]. They presented several methods published by other researchers for solving the same problem and compared those numerical solutions with their own solutions. The problem presented by Bertrand et al. was a square cavity (Fig. 8) filled with a solid material whose initial temperature T_0 was set equal to the melting temperature T_m. F8

The natural convection was initiated by exposing the left wall to a uniform temperature greater than the melting temperature when the material starts to melt at the left boundary. The top and bottom walls were kept insulated, and there was no magnetic field applied ($B_x = 0$). The physical properties of the molten steel, taken from the paper by Bertrand et al. [16] are given in Table 4. T4

Figures 9–12 show comparisons between the present numerical results and the numerical results presented by Bertrand et al. [16] for a grid with 90×90 cells at $t = 100$ s, 250 s, 1000 s, and 2500 s. In each figure, the position of the solidification front is plotted within the cavity, whose dimensions are normalized by the length, H. In Bertrand's article, several solutions from different methods were presented corresponding to each of the curves shown. One can note a good agreement between F9–F12

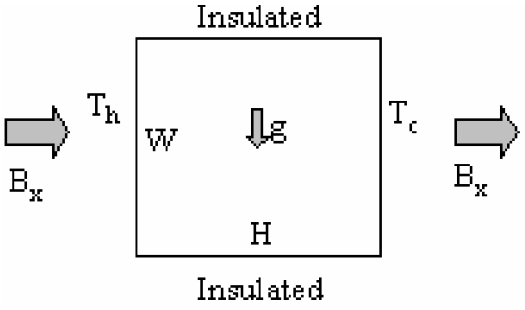

Figure 8 Geometry for the heat convection problem.

Table 4 Physical properties for steel [16]

$\rho = 7500\,\mathrm{kg\,m^{-3}}$	$L = 6 \times 10^4\,\mathrm{J\,kg^{-1}}$
$\alpha = 4 \times 10^{-5}\,\mathrm{m^2\,s^{-1}}$	$T_m = 232°\mathrm{C}$
$k = 60\,\mathrm{W\,m\,K^{-1}}$	$\Delta T = 3°\mathrm{C}$
$C_P = 200\,\mathrm{J\,kg\,K^{-1}}$	$\beta = 8.3 \times 10^{-4}\,\mathrm{K^{-1}}$
$\nu = 8 \times 10^{-7}\,\mathrm{m^2\,s^{-1}}$	$H = W = 0.10\,\mathrm{m}$

the present numerical results and Bertrand's solutions. Note that the solutions are all located in a range, and the present results are located within this range.

4.4. MHD Problem with Natural Convection

To validate our computer analysis code for situations in which natural convection is influenced by the magnetic field, we compared the present results with numerical results obtained by Ozoe and Okada [17]. In this problem, the flow is driven by two kinds of body forces: one due to thermal buoyancy in the y-momentum conservation equation and the other due to the presence of the magnetic field. The problem considered by Ozoe and Okada was a cubical cavity whose transverse section is shown in Fig. 8. Ozoe and Okada used the following parameters for silicon: $Pr = 0.054$, $Ra = 10^6$, $Ht = 0$, 300, and 500 where the Hartmann (Ht) number was given by Eq. (11) and the Prandtl (Pr), Rayleigh (Ra), and Grashoff (Gr)

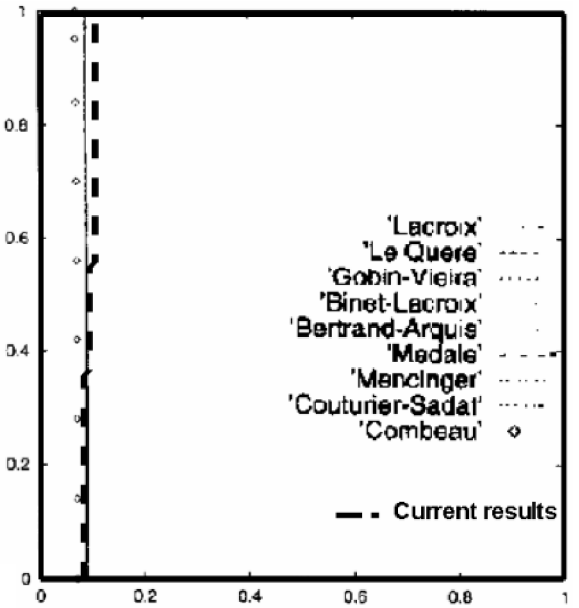

AQ1

Figure 9 Unsteady melting problem ($t = 100\,\mathrm{s}$): current results (dashed line) and a set of representative numerical results from other sources [16].

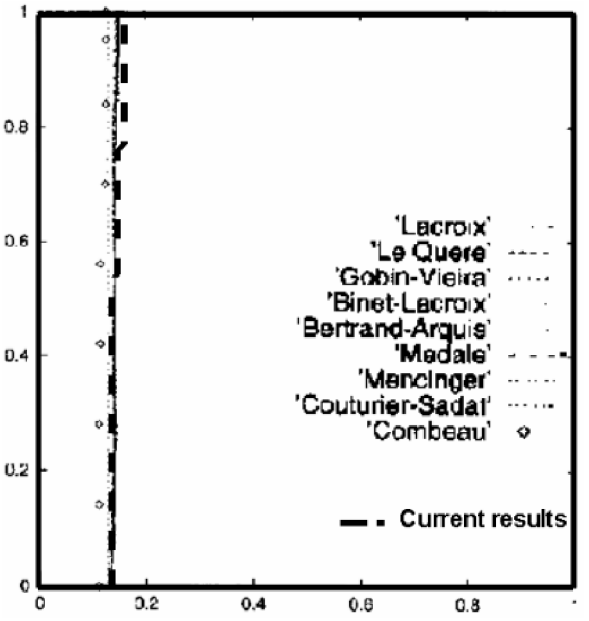

AQ1

Figure 10 Unsteady melting problem ($t = 250$ s): current results (dashed line) and a set of representative numerical results from other sources [16].

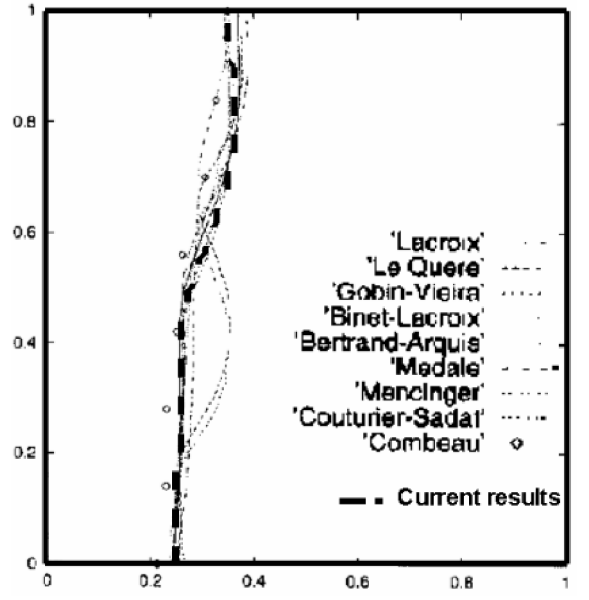

AQ1

Figure 11 Unsteady melting problem ($t = 1000$ s): current results (dashed line) and a set of representative numerical results from other sources [16].

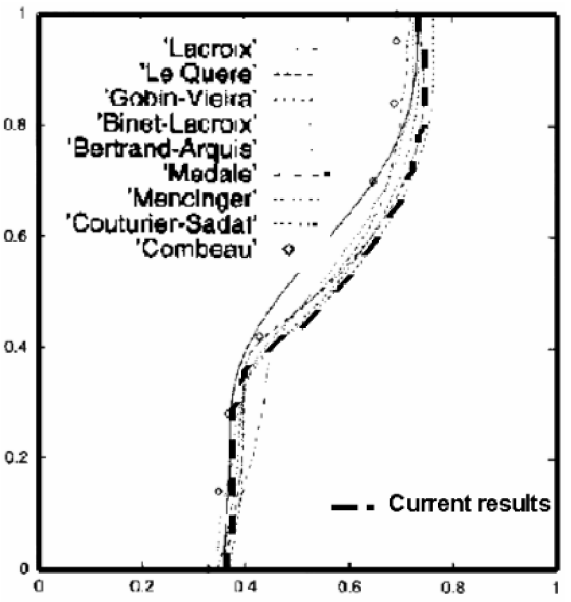

AQ1

Figure 12 Unsteady melting problem ($t = 2500\,\text{s}$): current results (dashed line) and a set of representative numerical results from other sources [16].

numbers are defined as

$$Pr = \frac{\mu}{\rho\alpha} \tag{19a}$$

$$Ra = Gr\,Pr \tag{19b}$$

$$Gr = \frac{g\beta(T_h - T_c)W^3}{\nu^2} \tag{19c}$$

The physical properties for silicon are the same as previously defined, except for viscosity, which, using the above parameters is obtained as $\mu = 0.00326346\,\text{kg m}^{-1}\,\text{s}^{-1}$. Choosing $W = 0.15\,\text{m}$ and $g = 9.81\,\text{m s}^{-2}$, we obtain $\Delta T = 6.54351\,\text{K}$. Then, for the various Ht numbers, we obtained different strengths of the uniform externally imposed magnetic field, Bo, as

$$Ht = 0 \qquad B_0 = 0.0\,T$$
$$Ht = 300 \qquad B_0 = 0.103019\,T$$
$$Ht = 500 \qquad B_0 = 0.171698\,T$$

Figures 13–15 show comparisons between the present results and those obtained by Ozoe and Okada. The figures show the isotherms obtained in the presence of magnetic field with Hartmann numbers equal to 0, 300, and 500. Note that, for $Ht = 0$, the problem reduces to the natural convection problem without any magnetic field applied. In Ozoe and Okada's article, the solutions were obtained with a grid size of 21×15 cells, whereas the current results were obtained with a grid size of 60×60 cells. One can notice that the results have a reasonable agreement.

F13–F15

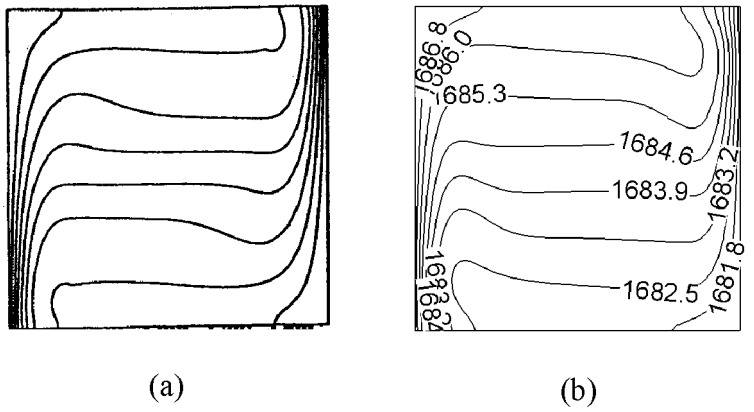

AQ1

Figure 13 Isotherms from Ozoe and Okada's [17] (a) and current (b) results ($Ht = 0$).

It is also interesting to note that as the Ht number is increased, the natural convection effects are gradually reduced.

5. HYBRID OPTIMIZATION ALGORITHM

The main objective of this work is to demonstrate how a robust optimization algorithm can be used to determine proper variation of magnetic field components on the walls of a solidification container so that desired features of the melt flow and/or the melt/solid interface can be achieved at each instant of time. One such robust optimizer is the hybrid optimization algorithm [18, 19] used in this work. It incorporates six popular optimization algorithms: genetic algorithm (GA), a quasi-Newton method of Pschenichny-Danilin (LM), modified Nelder-Mead simplex method (NM), sequential quadratic programming (SQP), Davidon-Fletcher-Powell gradient search algorithm (DP), and differential evolution

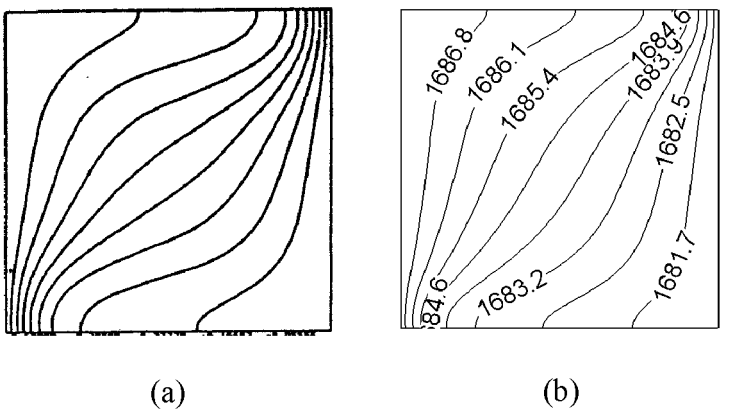

AQ1

Figure 14 Isotherms from Ozoe and Okada's [17] (a) and current (b) results ($Ht = 300$).

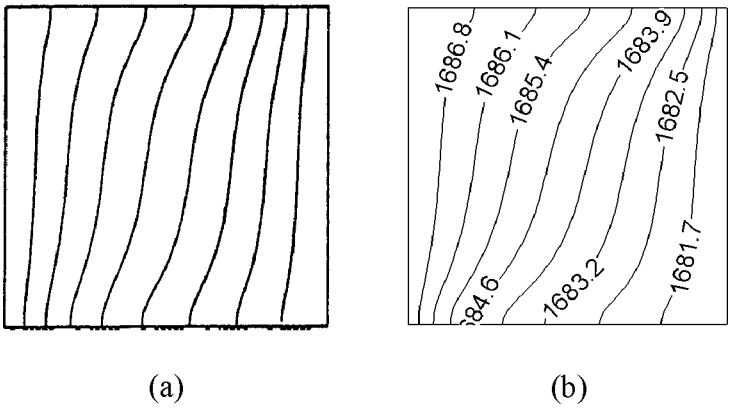

AQ1

Figure 15 Isotherms from Ozoe and Okada' [17] (a) and current (b) results ($Ht = 500$).

(DE). Each of these algorithms provides a unique approach to optimization with varying degrees of convergence, reliability, and robustness at different cycles during the iterative optimization procedure.

For example, the number of cost function evaluations per design iteration of a GA increases only mildly with the number of design variables, while increasing rapidly with the increased size of the initial population. In addition, the classical GA can handle constraints on the design variables, but it is not inherently capable of handling constraint functions. Thus, the brute force application of the standard GA to MHD optimization is economically unjustifiable.

The most serious drawback of the brute force application of the gradient search optimization is that the computing costs increase nonlinearly with the growing number of design variables, thus making these algorithms suitable for smaller optimization problems. Specifically, in a gradient-search optimization approach, the flow analysis code must be called at least once for each design variable during each optimization cycle to compute the gradient of the objective function if one-sided finite differencing is used for the gradient evaluation. If a more appropriate central differencing is used for the gradient evaluation, the number of calls to the flowfield analysis code will immediately double. Furthermore, during the optimization process with a typical gradient-based optimization algorithm, local minima can occur and halt the process before achieving an optimal solution.

In this case, the hybrid optimizer that we developed [18, 19] switches automatically to another method. That is, a set of analytically formulated heuristic rules and switching criteria were coded into the program to automatically switch back and forth among the different optimization algorithms as the iterative minimization process proceeded [18, 19] with the objective of accelerating the entire process and avoid premature termination in a local minima. Designs that violated constraints were automatically restored to feasibility via the minimization of the active global constraint functions. If at any time this constraint minimization failed, random designs were generated about the current design until a new feasible design was reached. The population matrix was updated every iteration with new designs and ranked according to the value of the objective function. The optimization

problem was completed when the maximum number of iterations or objective function evaluations were exceeded, or when the optimization program tried all individual optimization algorithms but failed to produce a nonnegligible decrease in the objective function.

6. INVERSE PROBLEM OF DETERMINING THE UNKNOWN MAGNETIC FIELD BOUNDARY CONDITIONS

In this article we deal with the inverse determination of the magnetic boundary conditions that give some pre-specified flowfield within some region [7, 19, 20]. Figure 16 shows the geometry and the boundary conditions for the test cases considered here. The height and length of the cavity filled with a melt were equal to 0.15 m. The top and bottom walls were kept thermally insulated. The left boundary was kept at a "hot" temperature, whereas the right wall was kept at a "cold" temperature. For the first test case, there was no phase change, because the "hot" and "cold" temperatures were above the melting temperature. F16

The four walls were subjected to unknown magnetic field distributions whose directions were made orthogonal to each wall. To satisfy the magnetic flux conservation equation

$$\nabla \bullet \mathbf{B} = 0 \tag{20}$$

the following periodic conditions were imposed

$$B_1(y) = B_2(y) \tag{21a}$$

$$B_3(x) = B_4(x) \tag{21b}$$

The objective was to minimize the natural convection effects by reducing the gradient of temperature along the y direction, thus trying to obtain a temperature profile similar to those obtained for pure conduction. The objective function to be

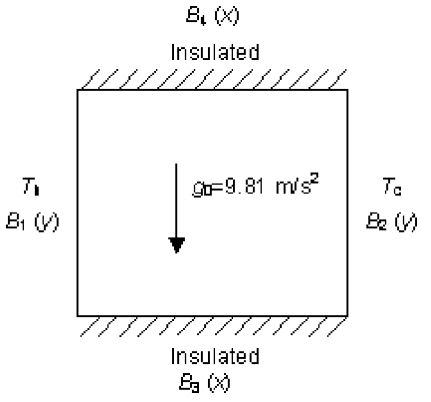

AQ1

Figure 16 Geometry and boundary conditions.

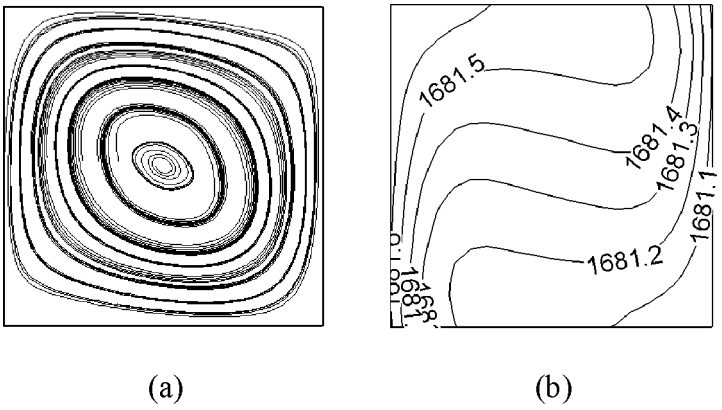

Figure 17 Streamlines a) and isotherms b) with $\mathbf{B} = 0$.

minimized was then formulated as [7]

$$F = \sqrt{\frac{1}{\#cells} \sum_{i=1}^{\#cells} \left(\frac{\partial T_i}{\partial y_i} \right)^2} \tag{22}$$

The magnetic field boundary conditions were determined at either four or six points equally spaced along each of the four boundaries and interpolated by using B-splines for the other points at those boundaries. The magnetic boundary conditions at right wall ($x = 0.15\,\mathrm{m}$) and the top wall ($y = 0.15\,\mathrm{m}$) of the container were then obtained by using periodic conditions from Eqs. (21a) and (21b). The physical properties were the same as previously used for the comparison with the Ozoe and Okada's article. For the first test case, the temperature difference $T_h - T_c$ was set equal to 0.654351 K, which gives a Rayleigh number of 10^5.

Figure 17 shows the velocity and temperature profiles predicted for the first test case without any magnetic flux applied and no phase change. Figure 18 F17 F18

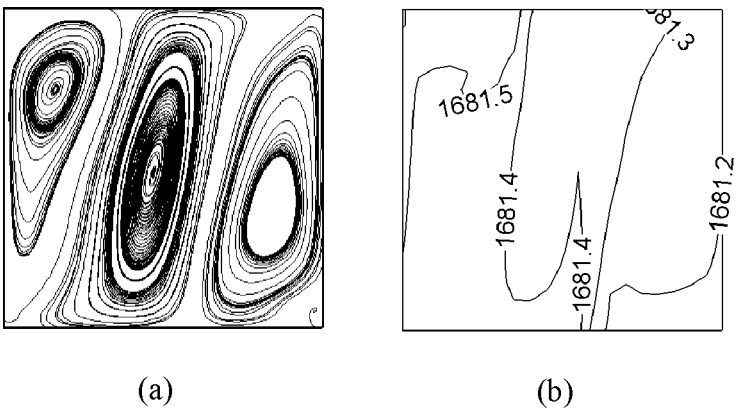

Figure 18 Streamlines a) and isotherms b) resulting from **B** optimized at four points per boundary.

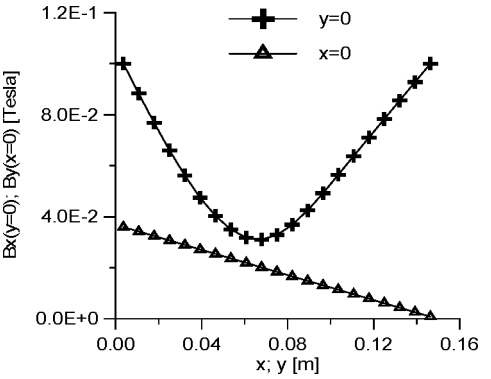

Figure 19 Optimized magnetic boundary conditions at $x = 0$ and $y = 0$ with the estimation of **B** at four points per boundary.

shows the optimized velocity and temperature profile using four points on each boundary for the estimation of the magnetic boundary conditions. One can see that the gradients of temperature in the y direction are reduced. Figure 19 shows F19 the optimized boundary conditions for $x = 0$ and $y = 0$, and Figure 20 shows the F20 convergence history of the process. One can see that the differential evolution (DE) algorithm did almost all the work.

Figure 21 shows the velocity and temperature profiles that result when six F21 terms are used in the B-spline on each boundary for the discretization of the magnetic boundary conditions, and these terms are optimized to minimize the objective function, Eq. (22). It is apparent that using more design variables (B-spline control points) in the optimization creates better results where the gradients of temperature in the y direction are further reduced.

Figure 22 shows the optimized boundary condition for $x = 0$ and $y = 0$, and F22 Figure 23 shows the convergence history of the process where one can see that the F23 differential evolution (DE) and genetic algorithm (GA) [21] optimization modules did almost all the work.

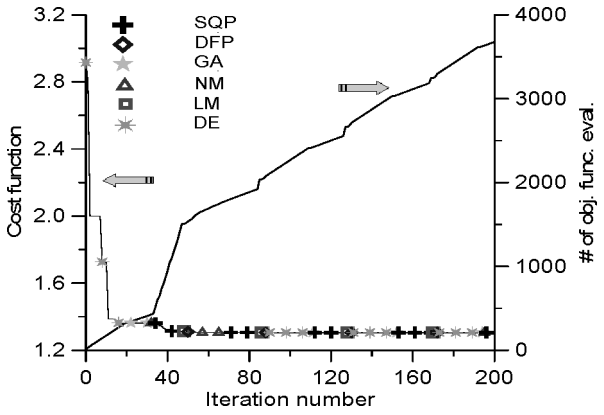

Figure 20 Optimization convergence history for the estimation of **B** at four points per boundary.

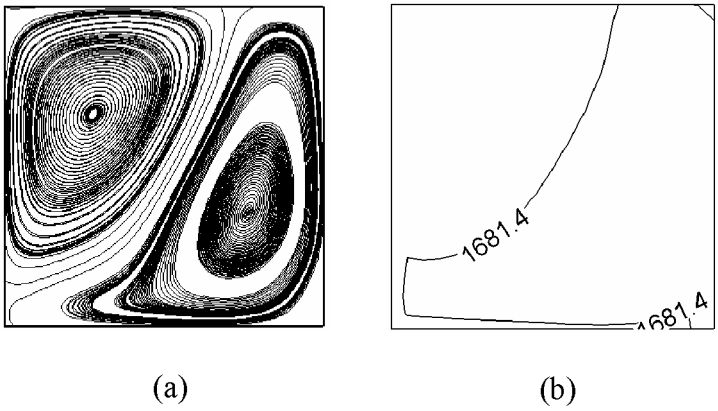

Figure 21 Streamlines (a) and isotherms (b) resulting from **B** optimized at six points per boundary.

The objective of the second test case was to minimize the curvature of the isotherms throughout the solidification process and especially at a prespecified time after the start of the solidification process. The following physical properties for silicon were used (Table 5) because appropriate values for steel were not available. T5

The temperature difference $T_h - T_c$ was set equal to 6.54351 K ($T_h =$ 1686.04351 K, $T_c = 1676.5$ K), and the length of the square container was taken as 0.069624 m, which gives a Rayleigh number of 10^5. The solidus and liquidus temperatures were equal to 1681.0 K and 1686.0 K, respectively. Thus, a mushy region exists between the phases. The initial condition was set as $T_0 = T_h$. Then, the solidification process without magnetic field started at the right wall, where $T = T_c$. The solidification front propagated toward the left wall accompanied by a strong recirculation of the remaining melt. Figure 24 shows the streamlines and isotherms F24 for this test case, predicted at 500 s.

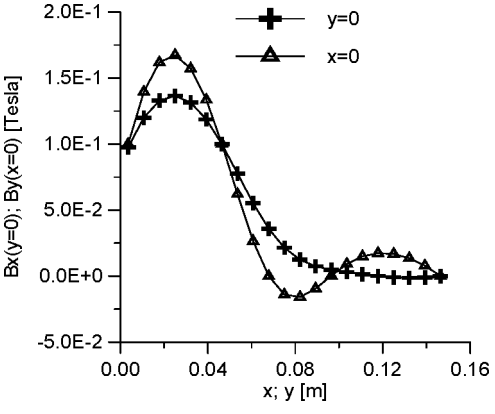

Figure 22 Optimized magnetic boundary conditions at $x = 0$ and $y = 0$ with the estimation of **B** at six points per boundary.

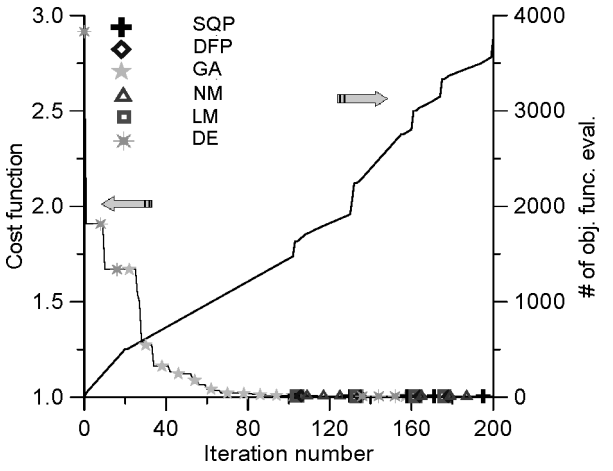

Figure 23 Optimization convergence history for the estimation of **B** at six points per boundary.

Table 5 Physical properties of molten and solid silicon

$\rho_l = 2550\,\mathrm{kg\,m^{-3}}$	$\rho_s = 2330\,\mathrm{kg\,m^{-3}}$
$k_l = 64\,\mathrm{W\,m^{-1}\,K^{-1}}$	$k_s = 22\,\mathrm{W\,m^{-1}\,K^{-1}}$
$C_{Pl} = 1059\,\mathrm{J\,kg^{-1}\,K^{-1}}$	$C_{Ps} = 1038\,\mathrm{J\,kg^{-1}\,K^{-1}}$
$\mu_l = 0.0032634\,\mathrm{kg\,m^{-1}\,s^{-1}}$	$\mu_s = 1.0 \times 10^3\,\mathrm{kg\,m^{-1}\,s^{-1}}$
$\sigma_l = 12.3 \times 10^5\,1/\mathrm{m}\ \Omega$	$\sigma_s = 4.3 \times 10^4\,1/\mathrm{m}\ \Omega$
$\beta = 8.3 \times 10^{-4}\,\mathrm{K^{-1}}$	$g = 9.81\,\mathrm{m\,s^{-2}}$
$\mu_m = 1.2566 \times 10^{-5}\,\mathrm{T\,m\,A^{-1}}$	$L = 1.803 \times 10^6\,\mathrm{J\,kg^{-1}}$

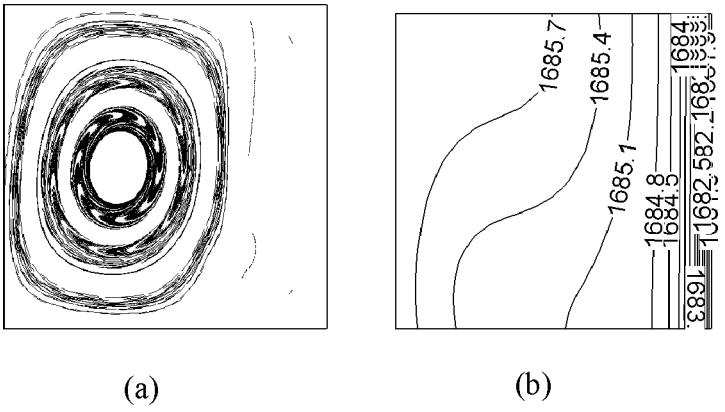

AQ1

Figure 24 Streamlines (a) and isotherms (b) at 500 s with $\mathbf{B} = 0$.

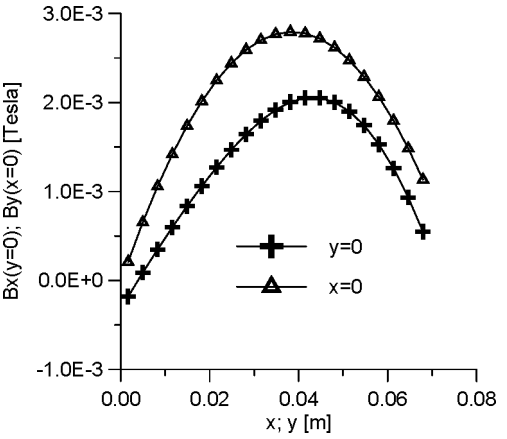

Figure 25 Streamlines a) and isotherms b) at 500 s resulting from the optimization of **B** at six points per boundary.

Figure 25 shows the streamlines and isotherms resulting from optimization of six B-spline points used for the discretization of the magnetic boundary conditions on each of the four walls so that solid/melt interface is as vertical as possible at each instant and especially at 500 s after the start of solidification. The boundary conditions at the other points on the walls were interpolated by using these B-splines. One can see that the resulting curvature of the isotherms in the melt and the solid for this MHD solidification test case is smaller than that in Fig. 24. F25

Figure 26 shows the optimized magnetic field boundary condition for $x = 0$ and $y = 0$ at 500 s, indicating that the strength of the externally applied magnetic field is quite low. Figure 27 shows the convergence history of the optimization process where one can see that the genetic algorithm (GA) [21] module did almost F26 F27

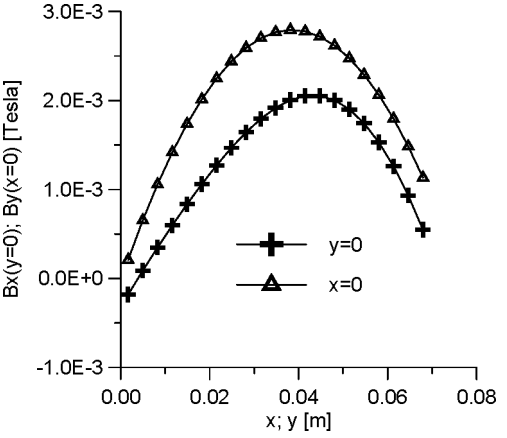

Figure 26 Optimized magnetic boundary conditions at 500 s with the estimation of **B** at six points per boundary.

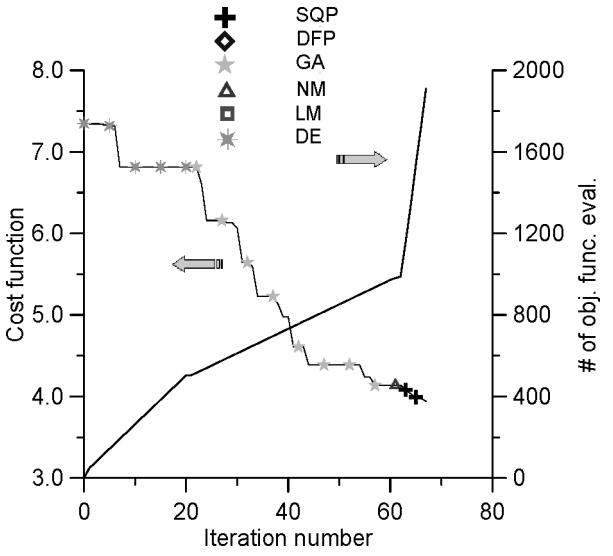

Figure 27 Optimization convergence history for the estimation of **B** at six points per boundary at 500 s.

all the work. The iterative process was forced to stop after 70 iterations due to the high computational cost involved.

7. CONCLUSIONS

In this article we have presented the results of a time-accurate MHD code that is capable of dealing with phase change problems. The code was validated against analytical and numerical (benchmark) results showing excellent agreement and was applied to test cases involving steady-state and unsteady solidification. The ability to minimize the natural convection effects in problems with and without phase change was demonstrated by determining an optimized distribution of magnetic filed along the boundaries of a container. A hybrid constrained optimization algorithm involving several evolutionary optimization modules with an automatic switching among them was used to determine unsteady boundary values of magnetic fields that were modifying the isotherms pattern to those similar to pure conduction problems. This de facto automatic control algorithm is directly applicable to solidification from a melt of arbitrary materials, including ferrous alloys, and is extendable to three-dimensional geometries.

ACKNOWLEDGMENTS

The first author is grateful for the postdoctoral fellowship received from University of Texas at Arlington and from CNPq, a Brazilian council for scientific and technological development. The second author is grateful for the partial support provided for this research on the grant NSF DMS-0073698 administered through the Computational Mathematics program.

The original paper was presented as "Reducing Convection Effects in Solidification by Applying Magnetic Fields Having Optimized Intensity Distribution" (by Colaco, M.J., Dulikravich, G.S. and Martin, T.J.), Keynote Lecture, ASME Paper HT2003-47308, ASME Summer Heat Transfer Conference, Las Vegas, NV, July 21–23, 2003.

REFERENCES

1. Motakeff, S. Magnetic field elimination of convective interference with segregation during vertical-Bridgman growth of doped semiconductors. J. Crystal Growth **1990**, *104*, 833–850.
2. Dulikravich, G.S.; Ahuja, V.; Lee, S. Modeling three-dimensional solidification with magnetic fields and reduced gravity. Int. J. Heat Mass Transfer **1994**, *37* (5), 837–853.
3. Dulikravich, G.S. Electro-Magneto-Hydrodynamics and Solidification. In *Advances in Flow and Rheology of Non-Newtonian Fluids, Part B*; Siginer, D.A., De Kee, D., Chhabra, R.P.; Eds.; Rheology Series, 8; Elsevier Publishers: 1999, 677–716. AQ2
4. Sampath, R.; Zabaras, N. A functional optimization approach to an inverse magneto-convection problem. Computer Methods Appl. Mech. Eng. **2001**, *190*, 2063–2097.
5. Fedoseyev, K.I.; Kansa, E.J.; Marin, C.; Ostrogorsky, A.G. Magnetic field suppression of semiconductor melt flow in crystal growth: Comparison of three methods for numerical modeling. JPN CFD J. **2001**, *9*, 325–333.
6. Dennis, B.H.; Dulikravich, G.S. Magnetic field suppression of melt flow in crystal growth. Int. J. Heat Fluid Flow **2002**, *23* (3), 269–277.
7. Dulikravich, G.S.; Colaço, M.J.; Dennis, B.H.; Martin, T.J.; Lee, S. Optimization of intensities and orientations of magnets controlling melt flow during solidification. J. Mater. Manuf. Processes **2004**, *19* (4), 695–718.
8. Voller, V.R.; Brent, A.D.; Prakash, C. The modeling of heat, mass and solute transport in solidification systems. Int. J. Heat Mass Transfer **1989**, *32*, 1719–1731.
9. Van Doormal, J.P.; Raithby, G.D. Enhancements of the SIMPLE method for predicting incompressible fluid flow. Numer. Heat Transfer **1984**, *7*, 147–163.
10. Raithby, G.D.; Torrance, K.E. Upstream-weighted differencing schemes and their application to elliptic problems involving fluid flow. Computers Fluids **1974**, *2*, 191–206.
11. Rappaz, M. Modelling of microstructure formation in solidification process. Int. Mater. Rev. **1989**, *34*, 93–123.
12. Colaço, M.J.; Orlande, H.R.B. Inverse forced convection problem of simultaneous estimation of two boundary heat fluxes in irregularly shaped channels. Numer. Heat Transfer–Part A **2001**, *39*, 737–760.
13. Colaço, M.J.; Orlande, H.R.B. In *Inverse Convection Problems in Irregular Geometries*, Proc. of the 21st Southeastern Conference on Theoretical and Applied Mechanics, Orlando, FL, March 12–15, 2002.
14. Woodson, H.H.; Melcher, J.R. *Electromechanical Dynamics Part III Elastic and Fluid Media*; John Wiley & Sons, Inc.: New York, 1968.
15. Özisik, M.N. *Heat Conduction*, 2nd Ed.; Wiley-Interscience; 1993. AQ2
16. Bertrand, O.; Binet, B.; Combeau, H.; Couturier, S.; Delannoy, Y.; Gobin, D.; Lacroix, M.; Le Quéré, P.; Médale, M.; Mencinger, J.; Sadat, H.; Vieira, G. Melting driven by natural convection—a comparison exercise: First results. Int. J. Thermal Sci. **1999**, *38*, 5–26.
17. Ozoe, H.; Okada, K. The effect of the direction of the external magnetic field on the three-dimensional natural convection in a cubical enclosure. Int. J. Heat Mass Transfer **1989**, *32*, 1939–1954.

18. Dulikravich, G.S.; Martin, T.J.; Dennis, B.H.; Foster, N.F. Multidisciplinary hybrid constrained GA optimization. In *EUROGEN'99—Evolutionary Algorithms in Engineering and Computer Science: Recent Advances and Industrial Applications*; Miettinen, K., Makela, M.M., Neittaanmaki, P., Periaux, J.; Eds.; Jyvaskyla, Finland, May 30–June 3, 1999, John Wiley & Sons: New York, 1999; 233–259. AQ3
19. Dulikravich, G.S.; Colaco, M.J.; Martin, T.J.; Lee, S. Magnetized fiber orientation and concentration control in solidifying composites. J. Composite Mater. **2003**, *37* (15), 1351–1366.
20. Dennis, B.H.; Dulikravich, G.S. Optimization of magneto-hydrodynamic control of diffuser flows using micro-genetic algorithm and least squares finite elements. J. Finite Elements Analysis Design **2001**, *37*, 349–363.
21. Chakraborti, N. Genetic algorithms in materials design and processing. Int. Mater. Rev. **2004**, *49*, 246–260.